



## Research Paper

## Multi-objective design of microvascular panels for battery cooling applications



Marcus Hwai Yik Tan<sup>a,d</sup>, Ahmad R. Najafi<sup>a,d,1</sup>, Stephen J. Pety<sup>b,d</sup>, Scott R. White<sup>c,d</sup>, Philippe H. Geubelle<sup>c,d,\*</sup>

<sup>a</sup> Department of Mechanical Science and Engineering, University of Illinois, Urbana, IL 61801, USA

<sup>b</sup> Department of Material Science and Engineering, University of Illinois, Urbana, IL 61801, USA

<sup>c</sup> Department of Aerospace Engineering, University of Illinois, Urbana, IL 61801, USA

<sup>d</sup> Beckman Institute for Advanced Science and Technology, University of Illinois, Urbana, IL 61801, USA

## HIGHLIGHTS

- Performed multi-objective design of microvascular battery cooling panels.
- Combined IGFEM gradient-based optimization with NNC method.
- Created Pareto front of maximum temperature and pressure drop.
- Designs optimized with prescribed pump power or prescribed flow rate.
- Optimizations performed with localized heating.

## ARTICLE INFO

## Keywords:

Battery cooling  
Optimization  
Multi-objective  
Interface-enriched generalized finite element method  
Microvascular composites  
Microchannel network

## ABSTRACT

Building on a recently developed optimization method based on an interface-enriched generalized finite element method, multiple objective functions are considered for the optimization of 2D networks of microchannels embedded in battery-cooling panels. The objective functions considered in this study are a differentiable alternative to the maximum temperature (the  $p$ -mean of the temperature), the pressure drop and the variance of the temperature. The  $\varepsilon$ -constraint method and the normalized normal constraint method are used to generate the pressure-temperature Pareto optimal front of the multi-objective optimization problem. The effects of different operating constraints/conditions such as localization of heat sources, prescribed pump power and imposed flow rate on the optimal designs are investigated. In addition to the topology of the embedded network, the cross sections of the microchannels are also introduced as design parameters to further improve the pressure drop of the designs. The resulting variable-cross-section optimized design is validated with experiment.

## 1. Introduction

Typical battery packaging found in electric vehicles consists of lithium-ion cells alternating with cooling panels and protective layers [1,2]. In operation, the cell pouches produce a substantial amount of heat that needs to be removed by active cooling. To prevent the deterioration of the battery, its temperature should be kept below approximately 40 °C [3]. Among the various strategies available for cooling, the most effective appears to be liquid cooling (see [4] for references) achieved by circulating a liquid coolant in channels embedded in panels typically made of aluminum. In addition to regulating

the battery temperature, the battery packaging also contains protective layers (typically, fiberglass or steel) that shield the battery from damage in the event of a crash.

A novel battery packaging system based on microvascular composites has been proposed recently [4,5]. In this approach, the battery cells are placed between microvascular composite panels, with each panel providing both active cooling and structural protection to the battery. Due to the high strength, stiffness and energy absorbing ability of carbon fiber composites, the proposed packaging is expected to provide superior crash protection at lower weight and volume compared to conventional packaging.

\* Corresponding author at: 306F Talbot Laboratory MC 236, 104 S. Wright, Urbana, IL 61801, USA.

E-mail address: [geubelle@illinois.edu](mailto:geubelle@illinois.edu) (P.H. Geubelle).

<sup>1</sup> Current address: Department of Mechanical Engineering and Mechanics, Drexel University, 3141 Chestnut St., Philadelphia, PA 19104, USA.

The design of the embedded channel network is a crucial factor in the performance of cooling panels. Many designs such as parallel, bifurcating/tree-like, serpentine, spiral, coiled and bifurcating-parallel hybrid have been proposed for cooling panels [6–9]. Computational tools such as topology optimization [10] and discrete topology optimization connecting lattice points in space [11] allow designs to be built from scratch. However, they often produce designs that appear too complicated for large-scale manufacturing. On the more theoretical side, the constructal theory has been proposed to guide the design [12]. However, parametric studies [13] and shape optimization [14,15] seem more promising in producing optimized designs suited for large-scale manufacturing.

This work builds on a previous study that used gradient-based shape optimization to design parallel networks [14]. In that study, one single objective function, a differentiable alternative to the maximum temperature referred to as the  $p$ -mean, was considered. In this work, we consider multiple objectives including  $p$ -mean, pressure drop and temperature variance. We also expand the breadth of the optimization technique by applying localized heat sources, comparing imposed coolant flow rate to imposed pumping power, and allowing for channel diameter to be a design variable.

The paper is organized as follows: in Sections 2 and 3, we summarize the dimensionally reduced hydraulic and thermal models, and the interface-enriched generalized finite element method (IGFEM) used for the analysis of the embedded network designs. We then describe in Section 4 the multi-objective optimization problem and the tools used to solve it. Starting in Section 5, we present the optimal designs based on various objective functions, constraints and thermal loads. In particular, we consider pressure drop across the network and  $p$ -mean of the temperature as objective functions/constraints in Section 5. Localized heat sources and pump power constraints are investigated in Section 6. Lastly, the set of design parameters is extended to include the size of the channel cross sections, and the temperature and pressure drop of the optimal design are validated experimentally in Section 7.

## 2. Hydraulic model

The dimensionally reduced model used herein has been described and validated in [14,16]. More information about the IGFEM used in this work can be found in [13,14,17–19]. For completeness, we provide in this section a brief summary of the thermal and hydraulic models, and of the numerical method used to solve them.

For brevity, the word “channel” hereafter refers to a microchannel. Consider a network of  $n_{ch}$  channels. Following the conventional analysis of pipe networks [20], the flow rates in the embedded channels are obtained using the classical hydraulics equations. Let  $g^{(i)}$  be the conductance of channel  $i$ . The relation between the contribution of channel  $i$  to the flow rates  $S_j^{(i)}$ ,  $S_k^{(i)}$  of the fluid entering the channel nodes  $j$ ,  $k$  and the nodal pressures  $P_j$ ,  $P_k$  is:

$$g^{(i)} \begin{bmatrix} 1 & -1 \\ -1 & 1 \end{bmatrix} \begin{Bmatrix} P_j \\ P_k \end{Bmatrix} = \begin{Bmatrix} S_j^{(i)} \\ S_k^{(i)} \end{Bmatrix}. \quad (1)$$

The conductance of a channel with a square cross section of width  $D$  or a circular cross section of diameter  $D$ , length  $L$  and a fluid kinematic viscosity of  $\nu$  is given by

$$g = \frac{CD^4}{\nu L}, \quad (2)$$

where  $C = 1/28.46$  and  $\pi/128$  for square and circular cross sections, respectively [21,22]. For rectangular cross sections,  $CD^4$  is replaced by  $\frac{a^3b}{4} \left( \frac{1}{3} - \frac{64a}{\pi^3b} \tanh \frac{\pi b}{2a} \right)$ , where  $a$ ,  $b$  respectively denote the height and width of the cross section [21]. The submatrices (1) for each channel can then be assembled into a global system of equations

$$[G]\{P\} = \{S\}, \quad (3)$$

where  $[G]$ ,  $\{P\}$  and  $\{S\}$  respectively denote the global conductivity matrix, nodal pressure vector and sink/source mass flow rate vector.

An aqueous ethylene glycol coolant is used in this study. To simplify the analysis, we assume that the fluid density is constant and equal to the average value over the temperature range in this study, i.e.,  $\rho = 1065 \text{ kg/m}^3$ . We further assume that the dynamic viscosity is uniform throughout the network, and has a temperature-dependence given by [23]

$$\mu(T) = 0.0069 \left( \frac{T}{273.15} \right)^{-8.3}, \quad (4)$$

where the temperature  $T$  is expressed in K and the dynamic viscosity in Pa·s. Unless specified otherwise, the dynamic viscosity is evaluated at the average temperature of the domain  $\Omega$ ,  $\langle T \rangle = \frac{1}{|\Omega|} \int_{\Omega} T d\Omega$ .

## 3. Dimensionally reduced thermal model and IGFEM

Instead of modeling the microchannels with finite diameters as in [13,17,24], we perform the analysis of the microvascular panel in 2-D and exploit the low diameter-to-length ratio to model them as line sources/sinks [18,25–27]. Consider a channel with cross-sectional area  $A$ , axial velocity  $u$ , average velocity  $u_{ave}$ , parametric coordinate along the channel  $s$ , mass flow rate  $\dot{m}$  and coolant specific heat capacity  $c_p$ . An energy balance over an infinitesimal segment of the channel readily yields the following expression for the heat flow rate per unit length:

$$q' = \dot{m}c_p \frac{dT_m}{ds}, \quad (5)$$

where  $T_m$  is the mixed-mean fluid temperature defined as  $T_m = \frac{1}{Au_{ave}} \int uT dA$  [28].

Let us denote by  $\kappa$ ,  $f(\mathbf{x})$ ,  $\tilde{h}$  and  $T_{amb}$  the thermal conductivity tensor of the solid, the distributed heat source, the convection coefficient and the ambient temperature, respectively. As shown in Fig. 1a, let the boundary of domain  $\Omega$  be consist of two parts, the Dirichlet boundary  $\Gamma_T$  with specified temperature  $T^{(p)}$  and the Neumann boundary  $\Gamma_q$  with prescribed heat flux  $q^{(p)}$ .  $\Omega$  consists of a solid part  $\Omega_s$  and a network of  $n_{ch}$  channels denoted by  $\Gamma_f^{(i)}$ . We further denote the unit tangent vector of channel  $i$  in the flow direction by  $\mathbf{t}^{(i)}$ , and the temperature field satisfying the Dirichlet boundary condition as  $T$ . With the assumption of  $T_m$  being approximately equal to the wall temperature  $T_w$ , the weak form of the problem is given by

$$0 = - \int_{\Omega_s} (\nabla \mathbf{v} \cdot \kappa \nabla T + \tilde{h} v T) d\Omega - \sum_{i=1}^{n_{ch}} \int_{\Gamma_f^{(i)}} v \gamma^{(i)} \mathbf{t}^{(i)} \cdot \nabla T d\Gamma + \int_{\Omega_s} v (f + \tilde{h} T_{amb}) d\Omega + \int_{\Gamma_q} v q^{(p)} d\Gamma, \quad (6)$$

$\forall v \in \mathbb{V}$ , where  $\mathbb{V}$  is the space of weight functions and  $\gamma^{(i)} = \dot{m}^{(i)} c_p$ .

In this study, the finite-dimensional space  $\mathbb{V}$  is constructed using the interface-enriched generalized finite element method (IGFEM), which allows for the use of a finite element mesh that does not necessarily conform to the geometry of the channel network as shown in Fig. 1a. The accuracy of the standard finite element method is recovered by enriching the space with properly constructed functions along the intersections of the channels with the elements to capture the weak discontinuity (i.e., gradient discontinuity) of the thermal field across the microchannels. In addition to greatly simplifying the meshing process, the IGFEM is particularly attractive for the shape-optimization study described in the next section since the stationary nature of the mesh avoids element distortion suffered by conventional finite-element-based shape optimization techniques.

IGFEM was first introduced by Soghrati et al. [29,30] to handle thermal problems with material interfaces. The original IGFEM handles an element cut by a material interface by considering multiple scenarios of intersection. Due to the large number of intersection scenarios for multiple interfaces in a single element, an algorithm was devised to

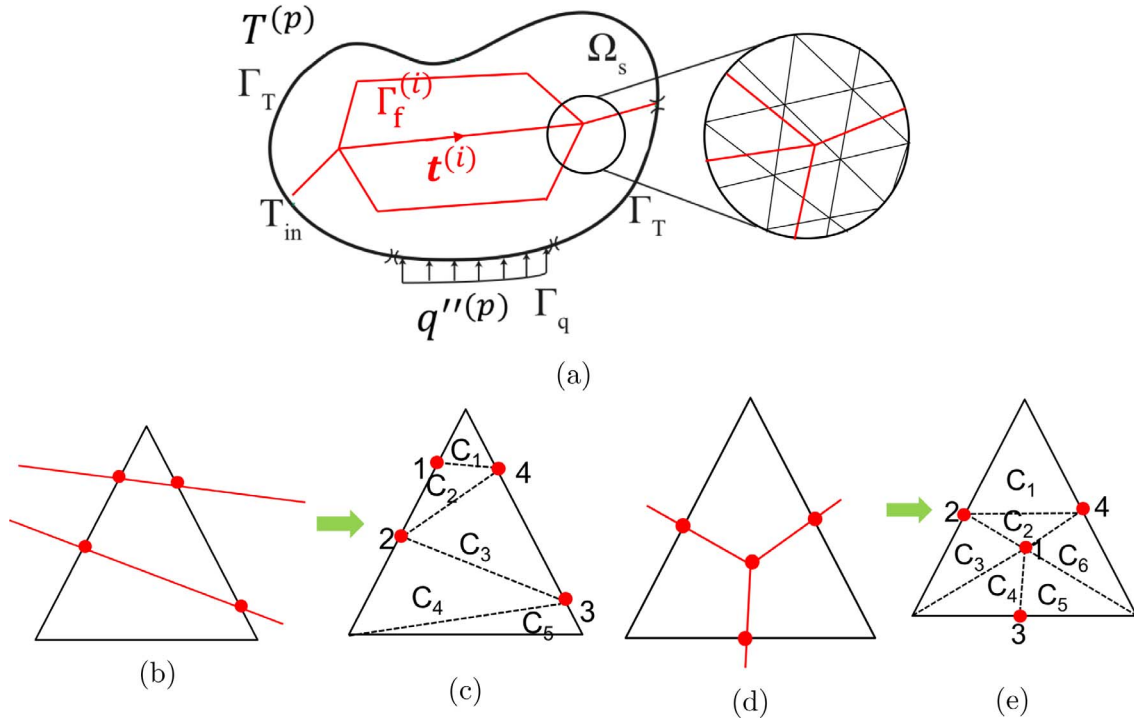


Fig. 1. (a) Schematic of the thermal problem, with the inset showing a portion of a non-conforming mesh. Element cut by multiple channels (b), and the associated integration subdomains and enriched nodes (b). Element containing a branch point (d), and the corresponding integration subdomains and enriched nodes (e).

simplify its implementation. This results in an extended version of IGFEM called hierarchical IGFEM [31,32]. In a nutshell, this algorithm works by considering each material interface recursively as if other material interfaces are not present. While the original IGFEM uses linear Lagrangian enrichment functions, other kinds of enrichment functions such as non-uniform rational B-splines (NURBS) [18,33] and higher-order Lagrangian enrichment functions [34] have also been developed.

For completeness, we next briefly introduce the IGFEM formulation, and describe the construction of enrichment functions relevant to this study. Let there be  $n_{on}$  original nodes in the non-conforming mesh, and let us denote the Lagrangian shape function associated with the original node  $i$  by  $N_i(\mathbf{x})$ . Further, let the nodal value at the original node be  $T_i$ . At the intersections between the channels and elements, examples of which are shown in Fig. 1b and d, enriched nodes indicated by red dots are introduced. Denote the number of enriched nodes in the non-conforming mesh by  $n_{en}$ , and the enrichment function associated with enrichment node  $j$  by  $\psi_j$ . We further introduce a generalized degree of freedom at the enrichment node  $j, \beta_j$ . The temperature field is then approximated by

$$T^{(h)}(\mathbf{x}) = \sum_{i=1}^{n_{on}} T_i N_i(\mathbf{x}) + \sum_{j=1}^{n_{en}} \beta_j \psi_j(\mathbf{x}). \quad (7)$$

Construction of the enrichment functions is illustrated by two scenarios shown in Fig. 1b and d. In the first scenario, an element is intersected by two channels. Enriched nodes are introduced at the intersections, and the integration subdomains (children elements) are created using Delaunay triangulation. The use of such a triangulation method greatly simplifies implementation, as the numerous intersection scenarios do not need to be considered separately. Associated with each of the enriched nodes 1–4 are the enrichment functions constructed from linear Lagrangian shape functions contained in the integration subdomains sharing the enriched nodes. Let us denote the shape function associated with node  $r$  in integration subdomain  $C_k$  by  $N_r^{C_k}$ . Then, the enrichment function associated with the enriched node  $j$  is given by

$$\psi_j = \sum_{k \in S_j} N_r^{C_k}, \quad (8)$$

where  $S_j$  is the set of integration subdomains sharing node  $j$ . For example, the enrichment functions associated with enriched node 2 of the first scenario (Fig. 1b) is  $\psi_2 = N_2^{C_2} + N_2^{C_3} + N_2^{C_4}$ .

In the second scenario where an element contains a branch point (Fig. 1d), an additional enriched node is introduced at the branch point along with the usual enriched nodes at the intersections with the element boundary. By (8), the enrichment function associated with enriched node 1 is  $\psi_1 = N_1^{C_2} + N_1^{C_3} + N_1^{C_4} + N_1^{C_5} + N_1^{C_6}$ . Details on the quadrature and stiffness matrix assembly can be found in [19].

#### 4. Optimization problem

In a typical design problem, multiple competing objectives need to be considered subject to a set of constraints. Let  $n_d$  and  $n_o$  respectively be the number of design parameters and objectives. Denoting the design parameters by  $\mathbf{d} = \{d_1, \dots, d_{n_d}\}$ , the nodal coordinates of the mesh by  $\mathbf{X}$ , the constraint functions as  $\mathbf{g}$  and the multiple objectives as a vector of functions  $\theta = \{\theta_1, \dots, \theta_{n_o}\}$ , the optimization problem can be formulated as:

$$\begin{aligned} \min_{\mathbf{d}} \quad & \theta(T(\mathbf{X}(\mathbf{d}), \mathbf{d}), \mathbf{X}, \mathbf{d}), \\ \text{such that} \quad & \mathbf{g}(T(\mathbf{X}(\mathbf{d}), \mathbf{d}), \mathbf{X}, \mathbf{d}) \leq 0. \end{aligned} \quad (9)$$

Since  $\theta$  in (9) ultimately depends only on  $\mathbf{d}$ , we henceforth write  $\theta = \theta(\mathbf{d})$ . Let  $\mathcal{F}$  be the set of feasible solutions to (9). As defined in [35], a solution  $\mathbf{x} \in \mathcal{F}$  dominates another solution  $\mathbf{y} \in \mathcal{F}$  if and only if  $\theta_i(\mathbf{x}) \leq \theta_i(\mathbf{y})$  for every  $i$  and  $\theta_j(\mathbf{x}) < \theta_j(\mathbf{y})$  for at least one  $j$ . Further, if no other solution in  $\mathcal{F}$  dominates  $\mathbf{x}$ , then  $\mathbf{x}$  is Pareto optimal. The set of all such solutions is called the Pareto optimal set and the Pareto optimal front is the set of objective values corresponding to the solutions in the Pareto optimal set. While some studies define a Pareto point as a Pareto solution, we define a Pareto point as a point on the Pareto optimal front. For brevity, we omit “optimal” when using the foregoing terms.

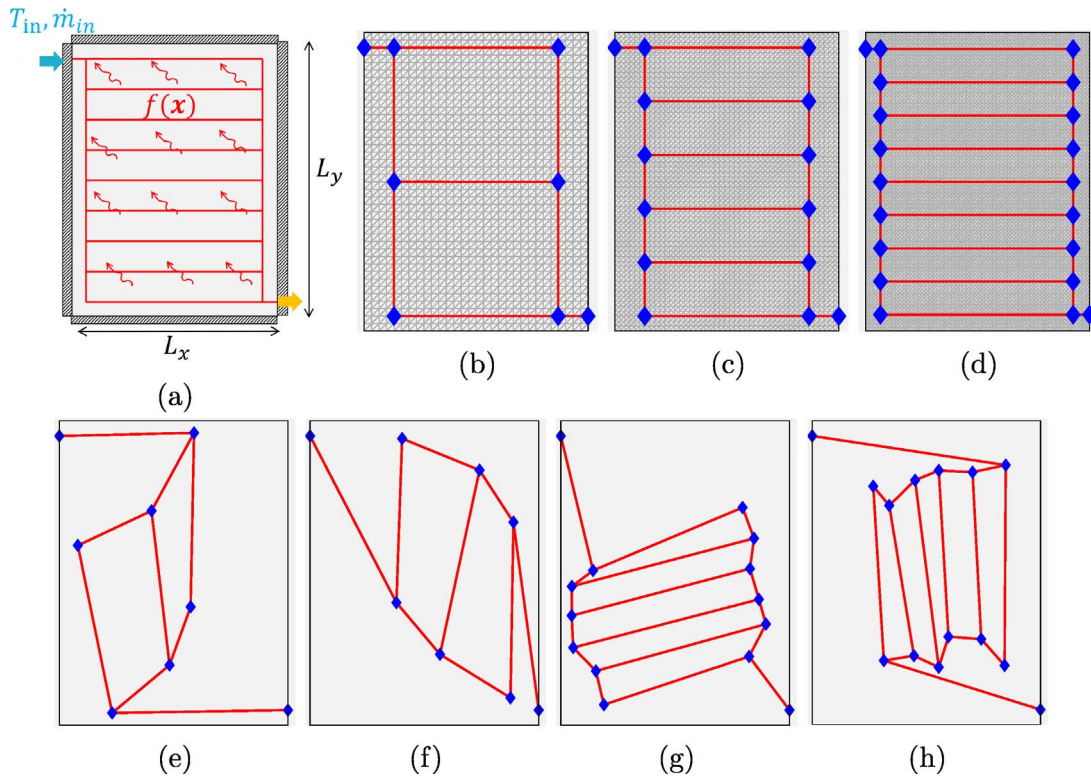


Fig. 2. (a) Channel design problem setup. Two-branch (b), five-branch (c) and eight-branch (d) reference networks with corresponding fixed background mesh. Examples of two-branch (e), (f) and five-branch (g), (h) initial designs.

#### 4.1. Problem setup

The optimization problem setup shown in Fig. 2a simulates the conditions experienced by a battery cooling panel in operation, which are similar to those used in a previous study [14]. A carbon fiber/epoxy matrix composite panel of size  $L_x = 0.15$  m,  $L_y = 0.2$  m is subject to a uniform thermal load of  $f(x) = 500$  W m $^{-2}$  unless stated otherwise. The composite is assumed to be a balanced plain weave with an isotropic in-plane conductivity. We set the thermal conductivity and thickness of the panel to be 2.7 W m $^{-1}$  K $^{-1}$  and 3 mm, respectively.

Embedded in the panel of Fig. 2a is a parallel network with coolant entering the inlet near the top left corner at a temperature of  $T_{in} = 27$  °C and exiting from the outlet near the bottom right corner. The parallel networks chosen to be optimized are the two-, five- and eight-branch networks shown in Fig. 2b–d with the corresponding non-conforming meshes. 48 randomly generated initial designs for each network geometry are used to address the problem of multiple local optima (some examples are shown in Fig. 2e–h). The geometrical constraints described in [14] are imposed to prevent the unphysical scenario of “self-crossing” of channels during the optimization process.

Unless mentioned otherwise, an optimal design is obtained by prescribing a mass flow rate of  $\dot{m}_{in} = 5 \times 10^{-4}$  kg/s (corresponding to a volumetric flow rate of 28.2 ml/min) at the inlet of the network and a zero reference pressure at the outlet. Under these boundary conditions, the system of hydraulics equations is linear in  $\{P\}$ . Since the viscosity is assumed uniform across the channel network, the flow rates are independent of the viscosity. Hence the hydraulics equations are decoupled from the heat equation and the actual pressure drop can be obtained after the heat equation is solved.

However, when the pump power is prescribed, the hydraulics and heat equations are coupled if the dynamic viscosity is temperature dependent. For this set of simulations, we decouple the equations by fixing the viscosity at  $2.34 \times 10^{-6}$  m $^2$ /s. This value corresponds to the viscosity evaluated at a temperature of 36 °C, which lies within the range of typical average panel temperatures.

#### 4.2. Generation of Pareto front

Multiple methods have been proposed to generate a Pareto front [36–40]. In the gradient-based optimization problem at hand, we adopt two decomposition-based methods. The first approach is the  $\varepsilon$ -constraint method [39], which minimizes one objective function called the primary objective function while imposing the others as constraints. The original problem (9) is then converted to:

$$\begin{aligned} \min_{\mathbf{d}} \quad & \theta_1(\mathbf{d}), \\ \text{such that} \quad & \mathbf{g}(\mathbf{d}) \leq 0, \\ \text{and} \quad & \theta_i(\mathbf{d}) \leq \varepsilon_i, \quad i = 2, \dots, n_o. \end{aligned} \quad (10)$$

The lower bound on  $\varepsilon_i$  can be obtained by performing single-objective optimization on  $\theta_i$ . When  $\varepsilon_i$  is sufficiently close to its lower bound, the  $\varepsilon_i$  constraint becomes active. However, as  $\varepsilon_i$  increases, the constraint eventually becomes inactive. Although simple in its implementation, this method does not typically produce well-distributed points on the Pareto front.

To overcome this limitation, we adopt as the second approach a boundary intersection method referred to as the normalized normal constraint (NNC) method [40]. The key idea of the method is to successively restrict  $\mathcal{F}$  to generate well-distributed solutions along the Pareto front. As illustrated in Fig. 3, the method in the bi-objective case can be summarized in the following two steps:

Step 1: Perform single-objective optimizations on  $\theta_1$  and  $\theta_2$ . Let the resulting solutions be denoted by  $\mathbf{d}^{1*}$  and  $\mathbf{d}^{2*}$ , respectively. Associated with these solutions are the end points of the Pareto front in the  $\theta_1$ - $\theta_2$ -plane:  $(\theta_1(\mathbf{d}^{1*}), \theta_2(\mathbf{d}^{1*}))$  and  $(\theta_1(\mathbf{d}^{2*}), \theta_2(\mathbf{d}^{2*}))$ . Now, let us define the normalized objective functions as

$$\begin{aligned} \tilde{\theta}_1 &= \frac{\theta_1(\mathbf{d}) - \theta_1(\mathbf{d}^{1*})}{\theta_1(\mathbf{d}^{2*}) - \theta_1(\mathbf{d}^{1*})}, \\ \tilde{\theta}_2 &= \frac{\theta_2(\mathbf{d}) - \theta_2(\mathbf{d}^{2*})}{\theta_2(\mathbf{d}^{1*}) - \theta_2(\mathbf{d}^{2*})}, \end{aligned} \quad (11)$$

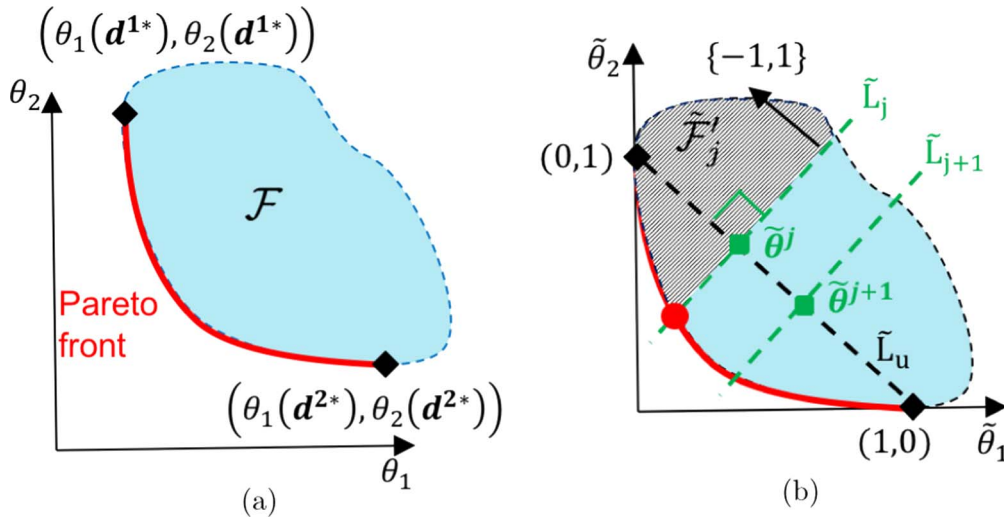


Fig. 3. Illustration of the normalized normal constraint method in the bi-objective case showing (a) the generation of the two end points of the Pareto front represented by the black diamonds, and (b) transformation to a normalized coordinate system followed by minimization of  $\tilde{\theta}_2$  in the new feasible region  $\tilde{\mathcal{F}}'_j$  to obtain a point (red circle) on the Pareto front.

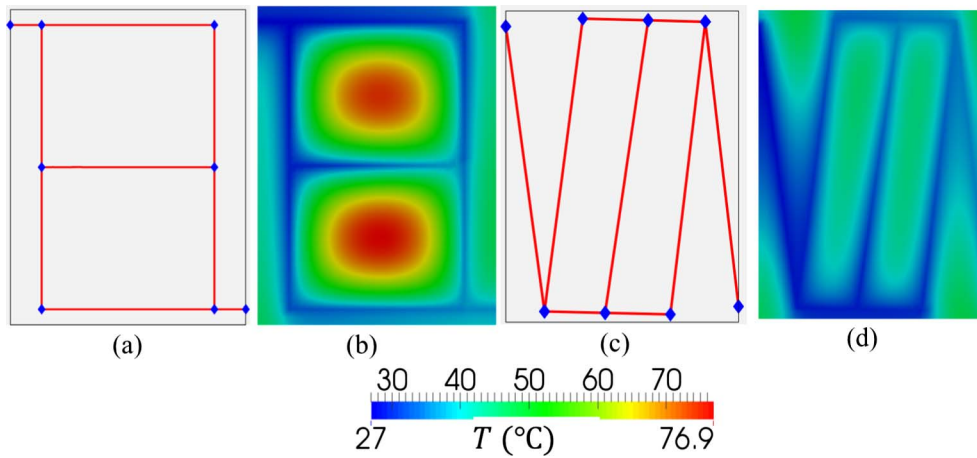


Fig. 4. Two-branch reference network (a) and network optimized with  $P_0 = 50$  kPa (c), and their respective thermal fields (b) and (d).

and the vector of normalized objective functions as  $\tilde{\theta} = \{\tilde{\theta}_1, \tilde{\theta}_2\}$ . In the  $\tilde{\theta}_1\tilde{\theta}_2$ -plane, the end points of the Pareto front are now  $\tilde{\theta}(d^{1*}) = (0,1)$  and  $\tilde{\theta}(d^{2*}) = (1,0)$ .

Step 2: To obtain the  $j$ -th Pareto point, where  $j = 2, \dots, N-1$ , we solve the following optimization problem:

$$\begin{aligned} \min_d \quad & \tilde{\theta}_2(d) \\ \text{such that} \quad & \mathbf{g}(d) \leq 0, \\ \text{and} \quad & \{-1, 1\}'(\tilde{\theta} - \tilde{\theta}^j) \geq 0, \end{aligned} \quad (12)$$

where

$$\tilde{\theta}^j := \frac{N-j}{N-1}(0,1) + \frac{j-1}{N-1}(1,0). \quad (13)$$

To understand the second constraint entering Eq. (12), let us denote the line connecting the two end points of the Pareto front in the normalized coordinate system by  $\tilde{L}_u$  as shown in Fig. 3b. Also, let  $\tilde{L}_j$  be the line perpendicular to  $\tilde{L}_u$  and passing through the point  $\tilde{\theta}^j$ . We observe that the second constraint restricts the solution to the side of the  $\tilde{L}_j$  indicated by the vector  $\{-1, 1\}$ , leading to a smaller feasible region  $\tilde{\mathcal{F}}'_j$ . Minimization of  $\tilde{\theta}_2$  in this new feasible region then produces a point on the Pareto front represented by the red dot in Fig. 3b. Since  $\tilde{L}_j$  is shifted in fixed increments along  $\tilde{L}_u$  as  $j$  increases, uniformly distributed points on the Pareto front are obtained. We note that the end point coordinates

of  $\tilde{L}_u$  are not critical for generating the interior points of the Pareto front. In fact, the role of  $\tilde{L}_u$  is only to allow for more uniform distribution of the points on the Pareto front. After the points on the Pareto front in the normalized coordinate system are obtained, the objective functions are transformed back into the original coordinate system.

Both (10) and (12) are solved with the sequential quadratic programming (SQP) algorithm [41] available in MATLAB. Since the abovementioned methods do not guarantee the generation of Pareto solutions, a Pareto filter described in [40] is used.

#### 4.3. Objective functions

As indicated earlier, the primary objective function used in this work is a differentiable alternative to the maximum temperature, the  $p$ -mean of the temperature field, defined as

$$\langle T \rangle_p = \left( \frac{1}{|\Omega|} \int_{\Omega} T^{(h)p} d\Omega \right)^{1/p}. \quad (14)$$

We set  $p = 8$ , the choice of which has been discussed in a previous study [14]. The sensitivity analysis on  $\langle T \rangle_p$  can also be found in that study.

Another objective function considered here is the pressure drop across the network. Since the outlet pressure is set to 0, the pressure drop is  $\Delta P = P_{in}$ , where  $P_{in}$  denotes the inlet pressure of the network. For simplicity, consider a single design parameter  $d$ . We differentiate

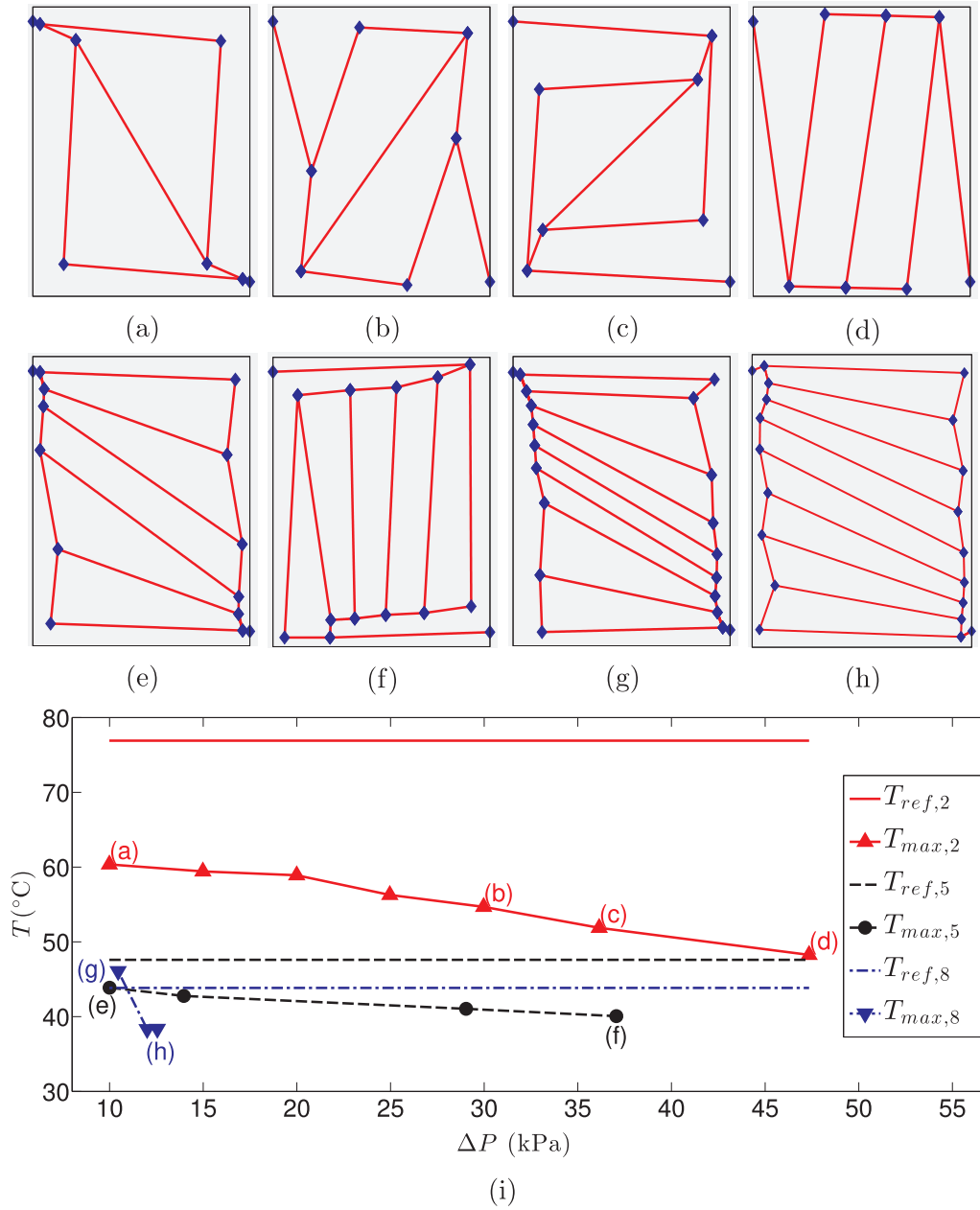


Fig. 5. (a)–(d) Two-branch optimal designs for  $\Delta P \leq 10, 30, 40, 50$  kPa. (e) and (f) Five-branch optimal designs for  $\Delta P \leq 10, 40$  kPa. (g) and (h) Eight-branch optimal designs for  $\Delta P \leq 10, 14$  kPa. (i) Maximum temperature as a function of the actual pressure drop for the two-, five- and eight-branch designs. The temperatures associated with the reference designs (Fig. 2(b)-(d)) are also indicated by horizontal lines for comparison.

the system of hydraulics Eqs. (2) to obtain the following system of equations that yields  $\partial(\Delta P)/\partial d$ :

$$[G] \left\{ \frac{\partial P}{\partial d} \right\} = - \left[ \frac{\partial G}{\partial d} \right] \{P\} + \left\{ \frac{\partial S}{\partial d} \right\}. \quad (15)$$

Due to the evaluation of the viscosity at the average temperature  $\langle T \rangle_1$ ,  $\partial[G]/\partial d$  can be calculated as

$$\left[ \frac{\partial G}{\partial d} \right] = \left[ \frac{\partial G}{\partial \nu} \right] \frac{\partial \nu}{\partial \langle T \rangle_1} \frac{\partial \langle T \rangle_1}{\partial d} + \sum_{i=1}^{n_{ch}} \left[ \frac{\partial G}{\partial L_i} \right] \frac{\partial L_i}{\partial d}. \quad (16)$$

The pressure drop may also be imposed as a constraint, i.e.,  $\Delta P \leq \Delta P_o$ , where  $\Delta P_o$  is the desired bound on the pressure drop.

The last objective function considered is the variance used as a measure of temperature uniformity in [15,10] and defined as

$$\sigma^2(T) = \frac{1}{|\Omega|} \left( \int_{\Omega} (T^{(h)} - \langle T \rangle_1)^2 d\Omega \right). \quad (17)$$

This expression can be rewritten as

$$\sigma^2(T) = \langle T \rangle_2^2 - \langle T \rangle_1^2, \quad (18)$$

which allows us to use the sensitivity analysis for  $\langle T \rangle_p$  derived in [14]. When the variance is chosen as the objective function, we want to impose a constraint  $T_{\max} \leq T_{\max,o}$ . Since this constraint cannot be handled by a gradient-based algorithm, we replace, as before,  $T_{\max}$  with  $\langle T \rangle_p$ . However, by doing so, we are left with the problem of finding an upper bound on  $\langle T \rangle_p$  corresponding to  $T_{\max,o}$ . To circumvent this issue, we correct for the difference between  $T_{\max}$  and  $\langle T \rangle_p$  in “real time” by adopting the algorithm proposed in [42]. Starting from an initial guess  $c^{(0)}$ , we impose the following constraint at each iteration  $i = 1, \dots, n$ :

$$c^{(i)} \langle T \rangle_p \leq T_{\max,o}, \quad (19)$$

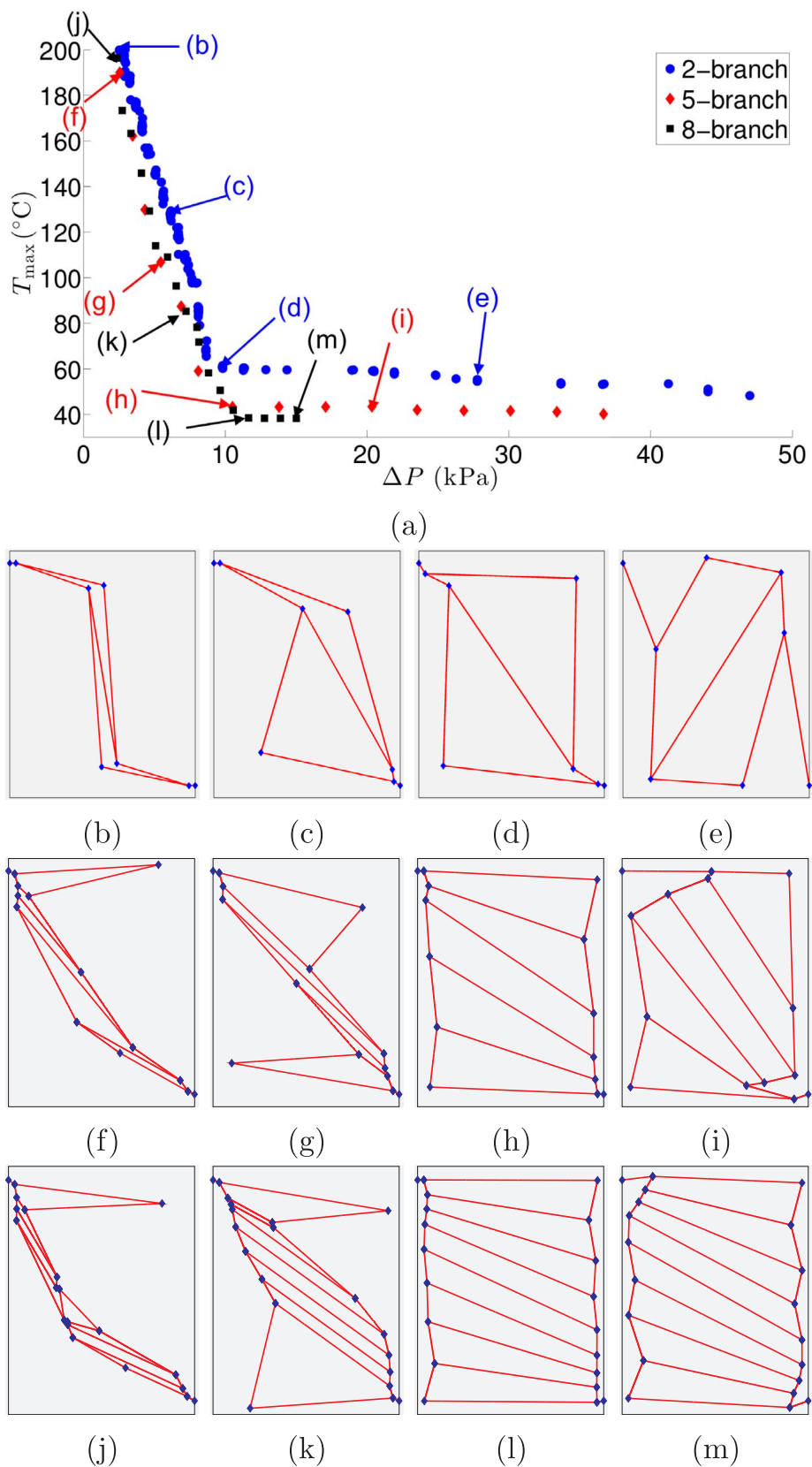


Fig. 6. (a) Tradeoff between  $T_{\max}$  and  $\Delta P$  represented by the Pareto fronts for the two-, five- and eight-branch networks, respectively. Some of the designs on the fronts are shown in (b)–(m). The two- and five-branch networks with the minimum value of  $T_{\max}$  on the fronts are shown in Fig. 5d and f.

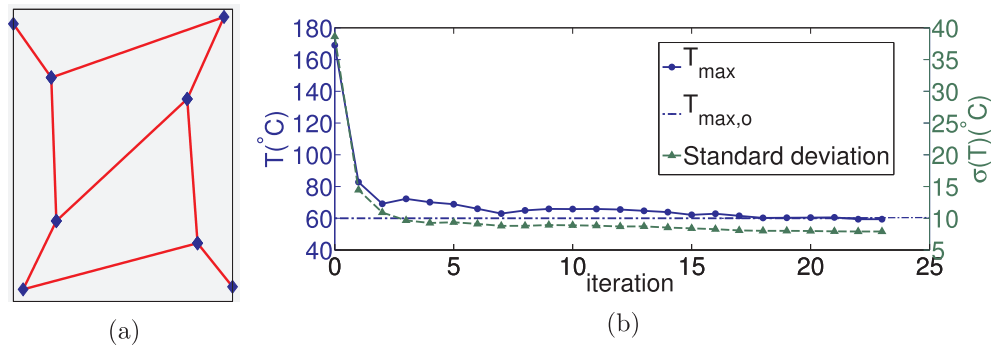


Fig. 7. (a) Optimal design obtained by minimizing the temperature variance with the constraints:  $\Delta P \leq 20$  kPa,  $T_{\max} \leq 60$   $^{\circ}\text{C}$ ; (b) corresponding optimization history.

where  $c^{(i)} = T_{\max}^{(i-1)} / \langle T \rangle_p^{(i-1)}$ .

## 5. Optimization results related to pressure and temperature

### 5.1. Pressure-temperature Pareto front from $\varepsilon$ -constraint method

To obtain the pressure-temperature Pareto front, we perform optimizations for different values of the upper bound of the pressure constraint  $P_0$ . Comparison of the temperature field associated with the two-branch reference network and that associated with the network optimized with  $P_0 = 50$  kPa in Fig. 4 shows a substantial reduction in the latter temperature due to the diagonal channels.

Fig. 5a–d presents the evolution of the optimal design for the two-branch network for  $P_0 = 10, 30, 40, 50$  kPa. When  $P_0$  is small, the optimal designs have small total channel length with only one interior channel placed diagonally across the panel (Fig. 5a). As  $P_0$  increases to 50 kPa, the optimal design becomes vertically oriented with three diagonally oriented interior channels spanning the panel (Fig. 5d). The optimal designs of the five-branch case follow the same trend when  $P_0$  increases from 10 to 40 kPa as shown in Fig. 5e and f. On the other hand, the eight-branch optimal designs for  $P_0 = 10$  and 14 kPa are both diagonally oriented (Fig. 5g and h).

The pressure-temperature Pareto front is presented as a plot of maximum temperature versus the actual pressure drop in Fig. 5i. Except for the eight-branch optimal design with  $P_0 = 10$  kPa, all optimal designs have a maximum temperature lower than the associated reference designs. For all branches, the pressure constraint becomes active at lower  $P_0$  and inactive at higher  $P_0$ . However, the value of  $P_0$  beyond which the pressure constraint becomes inactive decreases with increasing number of branches. While the pressure constraint becomes inactive at  $P_0 = 40$  kPa for the two-branch case, this transition occurs at  $P_0 = 14$  kPa for the eight-branch case. Furthermore, the lower pressure constraint seems to have a more detrimental effect on the performance of the network as the number of branches increases. As evident in Fig. 5i, the pressure and temperature range obtainable by the  $\varepsilon$ -constraint method is rather limited. As described next, this limitation can be overcome by the NNC method.

### 5.2. Pressure-temperature Pareto front from NNC method

Fig. 6a presents the maximum temperature/pressure drop Pareto fronts for the two-, five- and eight-branch networks. Each of these fronts is characterized by two distinct regions separated by a kink. When the pressure drop is low, the total length of the network is severely restricted, hence producing networks with little coverage of the panels as shown in Fig. 6b, c, f, g, j and k. Consequently, the temperature rises rapidly with decreasing pressure drop. On the contrary, when the pressure drop is allowed to be large, the networks have extensive coverage of the panels as evident from Fig. 6e, i and m, resulting in low maximum temperatures. For larger values of the pressure drop, increasing the pressure drop yields a small decrease in the maximum

temperature due to the restriction imposed by the panel size on the total network length. We note that this part of the front corresponds to the results shown in Fig. 5i. The networks presented in Fig. 6d, h and l corresponding to the kinks of the Pareto fronts thus represent a compromise between maximum temperature and pressure drop.

As the complexity of the network (i.e., the number of branches) increases, the Pareto front progressively moves closer to the origin. However, due to the saturation of the cooling effect of denser networks, this effect is relatively limited. This saturation effect is most prominent in the region before the kink, where the networks are restricted to a small area, and hence are highly dense. Indeed, no improvement is observed in the maximum temperature before the kink when the number of branches increases from five to eight.

### 5.3. Minimization of variance

In this subsection, we consider the minimization of the variance defined by (17) of the two-branch network subject to pressure and temperature constraints:  $T_{\max} \leq T_{\max,o}$  and  $\Delta P \leq P_0$ , where  $T_{\max,o} = 60$   $^{\circ}\text{C}$  and  $P_0 = 20$  kPa. The maximum temperature constraint is imposed using (19). In Fig. 7a and b, we show the optimal design with the lowest  $T_{\max}$  and corresponding optimization history of the maximum temperature and the standard deviation (square root of variance). The optimal design maximum temperature and actual pressure drop are respectively 59.4  $^{\circ}\text{C}$  and 18.5 kPa, which satisfy the imposed constraints.

We note, however, that the maximum temperature constraint algorithm did not work well sometimes due to the changing values of  $c^{(i)}$  in (19), which causes premature termination of the optimization. This prevents the enforcement of the constraint, and results in variances that are higher than those arising from the minimization of  $\langle T \rangle_p$ . Therefore, the minimization of  $\langle T \rangle_p$  appears to be a better choice for producing designs with a low maximum temperature while maintaining a uniform temperature distribution.

## 6. Optimization results related to operating constraints

### 6.1. Optimal designs with localized heat sources

Thermal management of lithium-ion batteries may need to consider localized heating due to abuse events. Furthermore, uneven charge/discharge profiles can cause concentration gradients in the electrolyte to develop, which then leads to localized heat generation [43]. As shown in this section, the computational design tool developed in this study allows for such heating to be considered. Provided that the distribution of the heat source can be approximated by a differentiable function, the sensitivity analysis described in [14] can be readily applied. For the purpose of demonstration, we define a heat source localized in  $n_r$  regions as

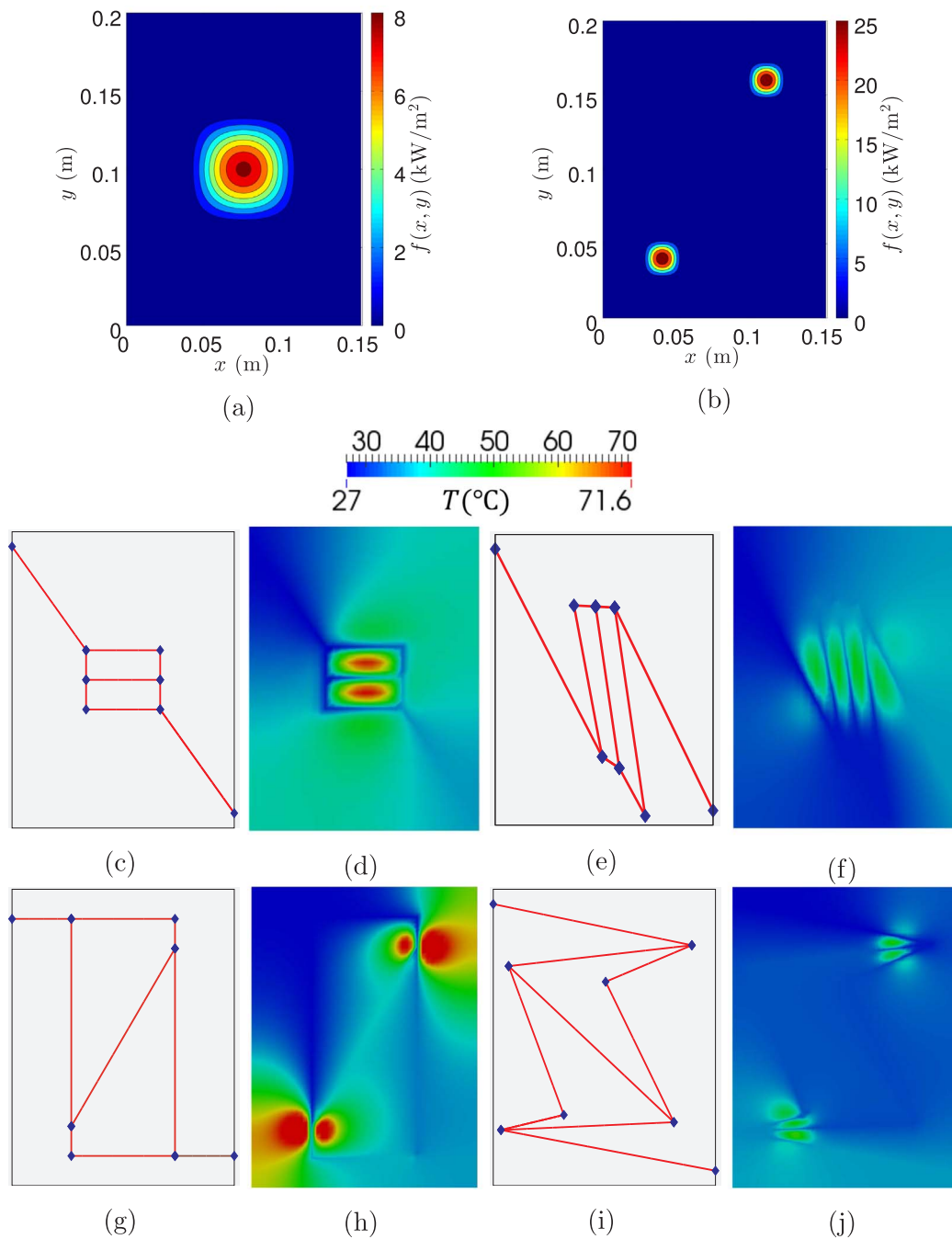


Fig. 8. Thermal loads on cooling panels represented by heat sources localized in the middle (a), and the top right and bottom left corners of the panel (b). Reference (c) and optimized (e) designs for heat source (a) and the associated temperature distributions (d) and (f). Reference (g) and optimal (i) designs for heat sources (b) with their corresponding thermal fields in (h) and (j).

$$f(x,y) = \begin{cases} q_o'' \sum_{i=1}^{n_r} \left[ 1 - \left( \frac{x-x_i}{r_i} \right)^2 \right]^2 \left[ 1 - \left( \frac{y-y_i}{r_i} \right)^2 \right]^2 & |x-x_i| \leq r_i, |y-y_i| \leq r_i, \forall i \\ 0 & \text{otherwise,} \end{cases} \quad (20)$$

with  $q_o''$  related to the total heat source  $Q = \int_{\Omega} f(x,y) d\Omega$  by the relation  $(256q_o'' \sum_i r_i^2)/225 = Q$ . We choose  $Q$  to be the total heat generated by the  $500 \text{ W m}^{-2}$  uniformly distributed heat source adopted in this work, i.e.,  $Q = 15 \text{ W}$ .

As shown in Fig. 8a and b, we consider two sets of parameters: (i)  $x_1 = 0.075 \text{ m}$ ,  $y_1 = 0.1 \text{ m}$ ,  $r_1 = 0.04 \text{ m}$  corresponding to a localized heat source in the middle, and (ii)  $x_1 = 0.04 \text{ m}$ ,  $y_1 = 0.04 \text{ m}$ ,  $x_2 = 0.11 \text{ m}$ ,  $y_2 = 0.16 \text{ m}$ ,  $r_1 = r_2 = 0.015 \text{ m}$ , corresponding to two heat sources

localized near the bottom left and top right corners of the domain. Fig. 8c–j compare the reference designs with the optimal designs for both cases. The reference designs fail to eliminate the hot spots as apparent in Fig. 8d and h. In contrast, the thermal fields associated with the optimized designs in Fig. 8f and j show that the hot spots are removed and the maximum temperatures are significantly reduced. Indeed, the maximum temperatures of the optimal designs are about  $20^\circ \text{C}$  lower than those of the reference designs.

### 6.2. Optimal designs with imposed pump power versus imposed flow rate

Thus far, the shape optimization of the embedded network was performed with a prescribed flow rate. In this section, we compare the

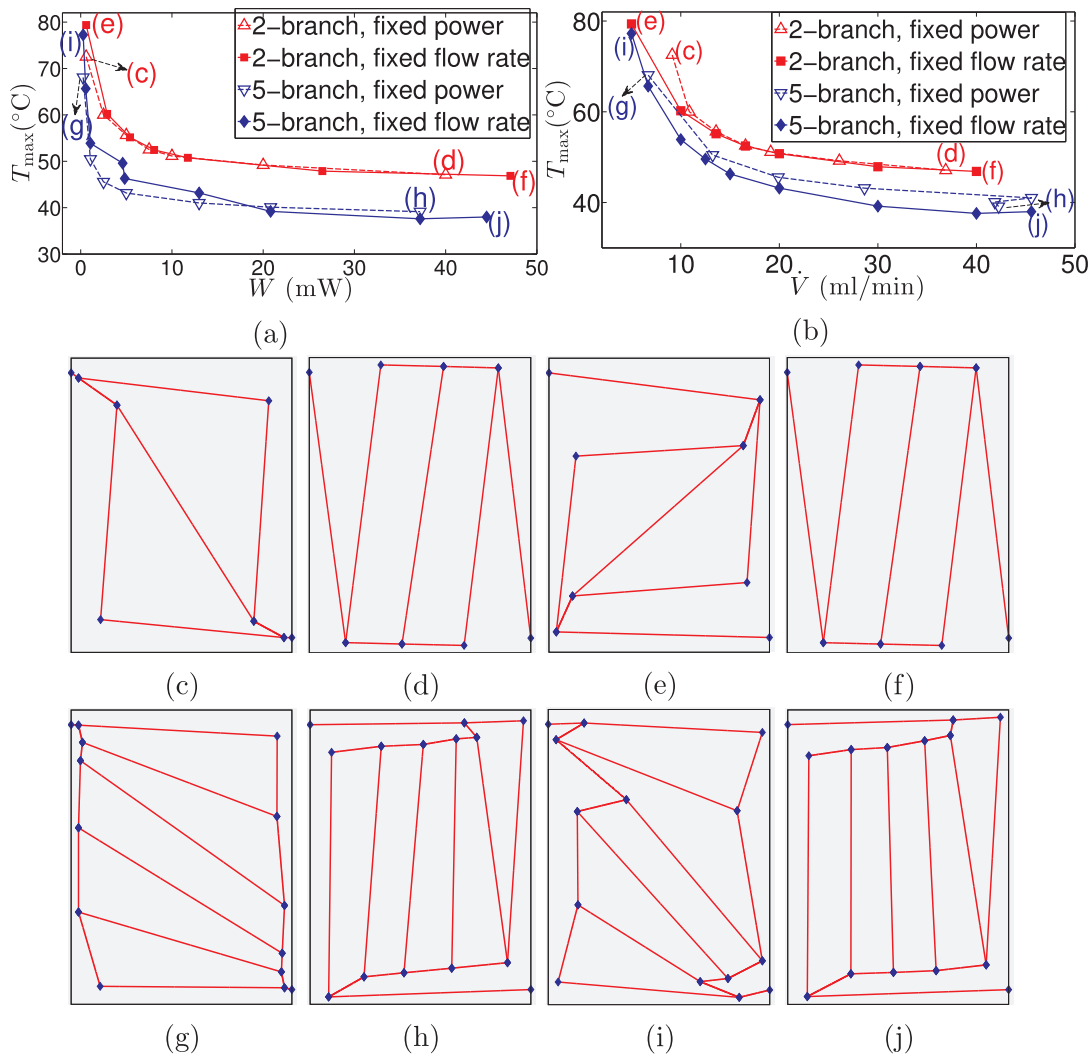


Fig. 9. Maximum temperatures associated with the 2- and 5-branch optimal designs as a function of (a) pump power and (b) flow rates, when the pump power or the flow rate is specified in the optimization. Designs optimized at low power (c), (g), and high power (d), (h). Designs optimized at low flow rate (e), (i), and high flow rate (f), (j).

optimal designs obtained with a prescribed pump power to those derived by prescribing the flow rate, both with constant viscosity evaluated at the reference temperature ( $2.34 \times 10^{-6} \text{ m}^2/\text{s}$  at  $36 \text{ }^\circ\text{C}$ ). Fig. 9a and b show the variation of the maximum temperature with respect to the pump power and flow rate, respectively. At low power, it is apparent that the fixed-power optimal designs have lower maximum temperatures compared with the fixed-flow-rate counterparts. Similar observation holds for the fixed-flow-rate optimal designs at low flow rates. The optimal designs corresponding to low prescribed power (Fig. 9c and g) are characterized by shorter channels since the prescribed power is akin to a pressure constraint.

For the two-branch case, the maximum temperature curves coincide with each other for high power as the fixed-power-optimal designs become identical to the fixed-flow-rate optimal designs (Fig. 9d and f) for sufficiently large power. The same trend holds for the fixed-flow-rate optimal designs at sufficiently large flow rates. The curves associated with the five-branch optimal designs are different, with the fixed-power optimal designs having higher maximum temperatures compared to the fixed-flow-rate optimal designs for  $W \geq 20 \text{ mW}$ . The reasons for this difference are twofold: (i) the optimized design at higher power (Fig. 9h) is not exactly the same as the design at high flow rates (9j), and (ii) optimization at high prescribed power is not accompanied by higher flow rates as shown in Fig. 9b. A closer examination of the five-branch fixed-power curve yields that the flow rates of the last three

points corresponding to optimization at a power greater than 13 mW stagnates at about 42 ml/min, indicating that the flow rates chosen at high power are only locally optimal.

## 7. Cross-sectional area as design parameter

### 7.1. Optimal designs

In Section 5, Fig. 6 showed that the pressure drop of the most “balanced” designs at the kinks (i.e., designs (d), (h) and (l) of Fig. 6) were rather insensitive to the number of branches. As shown next, the geometry of the channel cross sections can be introduced as design parameters to lower the pressure drop further. In this study, we fix the height of the channels at 0.75 mm but allow the width to vary between 0.35 and 1.5 mm to facilitate the manufacturing of the optimal designs. We then minimize  $\langle T \rangle_8$  of the eight-branch network subject to the constraints  $\Delta P \leq 7 \text{ kPa}$  and  $A_f \leq 0.041$ , where  $A_f$  is the area fraction of the network. The upper bound of  $A_f$  is chosen to be the area fraction of the fixed-cross-section optimal network in Fig. 6l, for which the width = 0.75 mm and  $\Delta P = 10.6 \text{ kPa}$ . The resulting variable-width optimal design is shown in Fig. 10a together with the widths of its channels. It is observed that larger cross sections are favored for shorter channels near the boundaries of the domain, hence lowering the pressure drop and maximum temperature. Indeed, the pressure constraint of

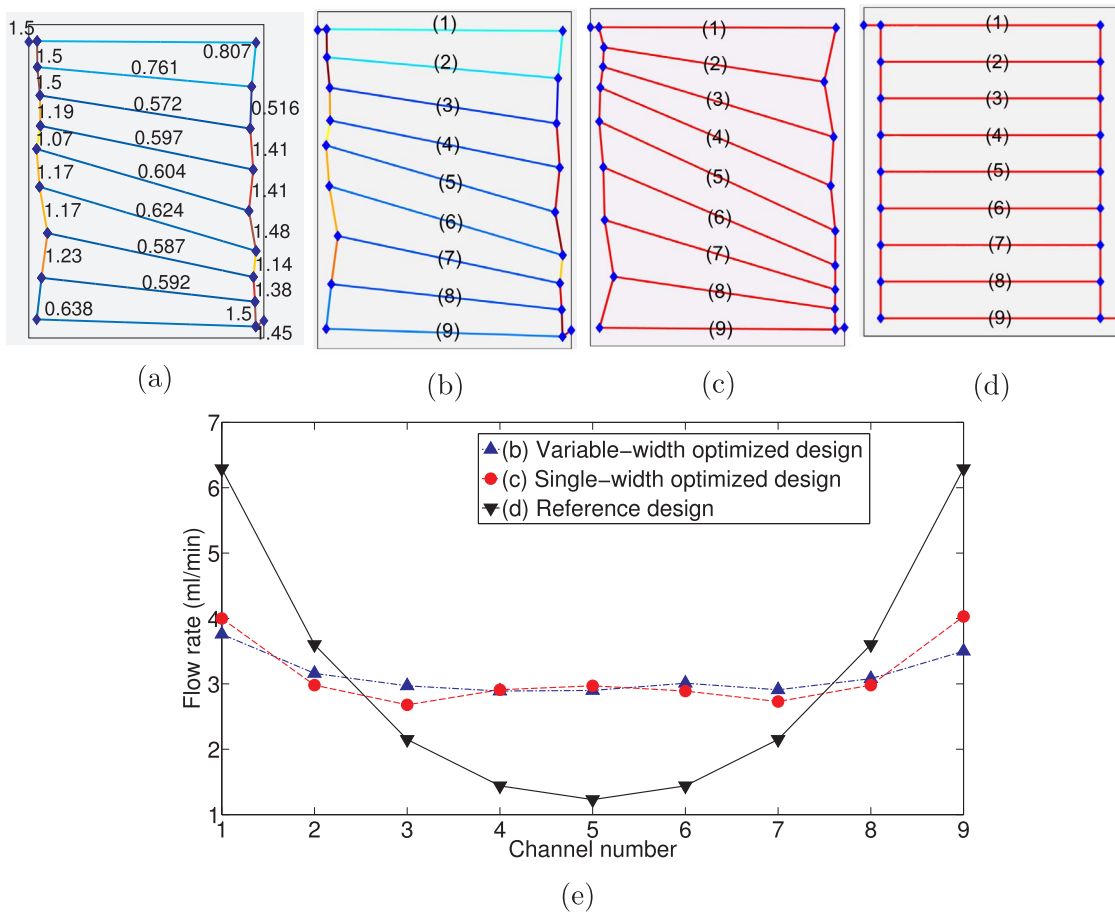


Fig. 10. Introducing the width of the channel rectangular cross sections as design variables allows further reduction in pressure drop and improves thermal performance compared with the fixed-cross-section case. (a) Widths in mm of the variable-width optimal design. (b) Variable-width optimal design with  $T_{max} = 38.3\text{ }^{\circ}\text{C}$ ,  $\Delta P = 7.0\text{ kPa}$  and  $A_f = 0.041$ . (c) Fixed-cross-section optimal design (same as Fig. 6f) with  $T_{max} = 41.9\text{ }^{\circ}\text{C}$ ,  $\Delta P = 10.6\text{ kPa}$  and  $A_f = 0.041$ . (d) Reference design. (e) Flow rates in the 9 interior channels of (b)–(d).

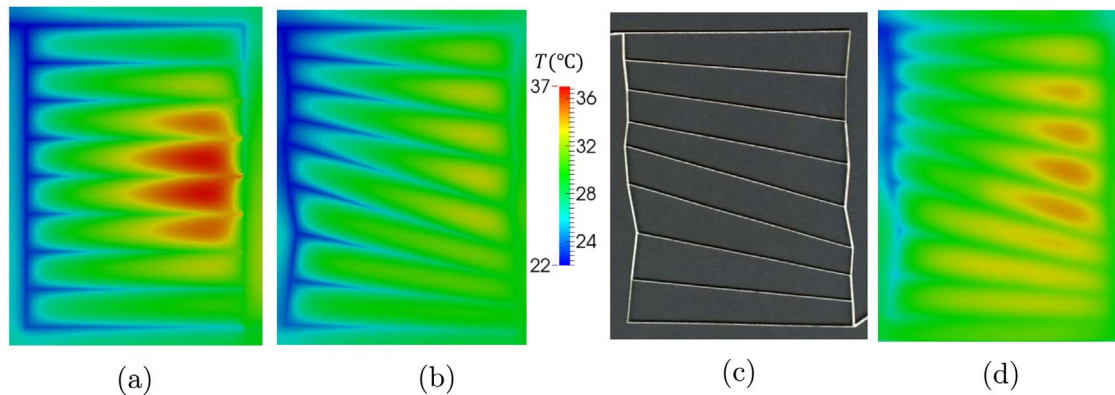


Fig. 11. Computed temperature distributions associated with the reference eight-branch network with fixed cross section (a) and with the optimized eight-branch network with variable channel diameters (b). (c) Laser-cut sacrificial template used to embed the optimal eight-branch network in the composite panel for the validation study. (d) Experimentally measured temperature distribution of the optimized network.

7.0 kPa is satisfied by the variable-width network. Therefore, introducing the cross-sectional geometry of the channels as design parameters results in further reduction in pressure drop compared with the fixed-cross-section optimization.

As shown in Fig. 10e, both variable-width and fixed-cross-section optimal designs tend to equalize the flow rates in the interior channels labeled in Fig. 10b and c. In contrast, the distribution of the flow rates of the same channels of the reference network is rather non-uniform.

### 7.2. Validation

In this last section, we present a validation study of the variable-width optimal design under the thermal loading conditions described in the validation exercise of [14] and for the same flow rate of 28.2 ml/min. The temperature of the reference design (Fig. 11a) is significantly less uniform than that of the optimized design (Fig. 11b). While the average and maximum temperatures associated with the former are respectively 30.4 °C and 37.2 °C, those associated with the latter are 27.9 °C and 32.9 °C, respectively.

Using the laser-cut sacrificial template shown in Fig. 11c, a microvascular composite panel with the optimized network was fabricated. The thermal field measured experimentally with an infrared (IR) camera shown in Fig. 11d agrees quite well with the simulated thermal solution: the measured average and maximum temperatures are 30.0 °C and 34.6 °C, respectively. The simulated average and maximum temperatures are respectively lower than the corresponding measured temperatures by 2.1 °C and 1.7 °C due to an assumption of the thermal model, i.e, the mixed-mean temperature of the coolant is approximately equal to the channel wall temperature [14,16]. In reality, the mixed-mean temperature is lower than the wall temperature. Furthermore, the measured pressure drop of 9.0 kPa is slightly higher than its simulated counterpart of 8.15 kPa since the fluid model neglects the pressure loss at the branches and corners of the channel network.

## 8. Conclusions

Building on a recently developed computational tool for the gradient-based design of microvascular panels for active cooling applications, we considered two competing objective functions —  $p$ -mean of the temperature and pressure drop — in the optimization of parallel microchannel networks. The Pareto front associated with these competing objectives was generated using the  $\epsilon$ -constraint and NNC methods. The former method generated a front that showed a rather slow decrease in maximum temperature with respect to the pressure drop. This front turned out to be part of the complete front generated by the NNC method, which showed two distinct regions separated by a kink. One region showed a slow decrease of the maximum temperature as the pressure drop increased, consistent with the results obtained with the  $\epsilon$ -constraint method. The other region was characterized by a steep slope indicating a rapid rise in the maximum temperature as the pressure was reduced. The shape optimization tool was also applied with variance of the thermal field as an objective function.

We also optimized the network designs in the presence of localized heat sources. These optimal designs were superior to the “ad hoc” reference designs under these specific thermal loads. Optimization with prescribed pump power and constant fluid viscosity were also performed. However, the tendency of designs optimized at higher pump power to operate at lower flow rates and the constant viscosity assumption placed power-based optimization at a disadvantage compared with the more versatile fixed-flow-rate optimization.

Finally, we showed that the pressure drop of the network could be improved substantially when the sizes of the channel cross sections were introduced as design parameters. We then validated the variable-width optimal design with experimental IR measurements.

## Acknowledgements

This work has been supported by the DEMS Program of the NSF Division of Civil, Mechanical and Manufacturing Innovation (Award No. 1436720); the Air Force Office of Scientific Research National Defense Science and Engineering Graduate (NDSEG) Fellowship (32 CFR 168a) and the Center for Electrical Energy Storage funded by DOE Office of Basic Energy Sciences (Grant No. 615 DOE ANL 9F-31921). The authors wish to thank Prof. Nancy Sottos for providing useful feedback on this study.

## References

- [1] S. Jayaraman, G. Anderson, S. Kaushik, P. Klaus, Modeling of Battery Pack Thermal System for a Plug-in Hybrid Electric Vehicle, Tech. Rep. 2011-01-0666, SAE, 2011.
- [2] H.S. Hamut, I. Dincer, G.F. Naterer, Experimental and theoretical efficiency investigation of hybrid electric vehicle battery thermal management systems, *J. Energy Resour. Technol.* 136 (2014) 011202.
- [3] J. Neubauer, E. Wood, Thru-life impacts of driver aggression, climate, cabin thermal-management and battery thermal management on battery electric vehicle utility, *J. Power Sources* 259 (2014) 262–275.
- [4] S.J. Pety, M.H.Y. Tan, A.R. Najafi, P.R. Barnett, N.R. Sottos, P.H. Geubelle, S.R. White, Carbon fiber composites with 2D microvascular networks for battery cooling, *Int. J. Heat Mass Transfer* 115 (2017) 513–522.
- [5] S. Pety, P. Chia, S. Carrington, S. White, Active cooling of microvascular composites for battery packaging, *Smart Mater. Struct.* 26 (2017) 105004.
- [6] S.M. Senn, D. Poulikakos, Laminar mixing, heat transfer and pressure drop in tree-like microchannel nets and their application for thermal management in polymer electrolyte fuel cells, *J. Power Sources* 130 (2004) 178–191.
- [7] J.C. Kurnia, A.P. Sasmito, A.S. Mujumdar, Numerical investigation of laminar heat transfer performance of various cooling channel designs, *Appl. Therm. Eng.* 31 (2011) 1293–1304.
- [8] S.M. Baek, S.H. Yu, J.H. Nam, C.J. Kim, A numerical study on uniform cooling of large-scale PEMFCs with different coolant flow field designs, *Appl. Therm. Eng.* 31 (2011) 1427–1434.
- [9] B. Ramos-Alvarado, P. Li, H. Liu, A. Hernandez-Guerrero, CFD study of liquid-cooled heat sinks with microchannel flow field configurations for electronics, fuel cells and concentrated solar cells, *Appl. Therm. Eng.* 31 (2011) 2494–2507.
- [10] T. Matsumori, T. Kondoh, A. Kawamoto, T. Nomura, Topology optimization for fluid-thermal interaction problems under constant input power, *Struct. Multidiscipl. Optim.* 47 (2013) 571.
- [11] A.M. Aragón, J.K. Wayer, P.H. Geubelle, D.E. Goldberg, S.R. White, Design of microvascular flow networks using multi-objective genetic algorithms, *Comput. Meth. Appl. Mech. Eng.* 197 (2008) 4399–4410.
- [12] A. Bejan, S. Lorente, Constructal theory of generation of configuration in nature and engineering, *J. Appl. Phys.* 100 (2006) 041301.
- [13] S. Soghrati, P.R. Thakre, S.R. White, N.R. Sottos, P.H. Geubelle, Computational modeling and design of actively-cooled microvascular materials, *Int. J. Heat Mass Transfer* 55 (2012) 5309–5321.
- [14] M.H.Y. Tan, A.R. Najafi, S.J. Pety, S.R. White, P.H. Geubelle, Gradient-based design of actively-cooled microvascular composite panels, *Int. J. Heat Mass Transfer* 103 (2016) 594–606.
- [15] A. Jarrett, I.Y. Kim, Design optimization of electric vehicle battery cooling plates, *J. Power Sources* 196 (2011) 10359–10368.
- [16] M.H.Y. Tan, P.H. Geubelle, 3D dimensionally reduced modeling and gradient-based optimization of microchannel cooling networks, *Comput. Meth. Appl. Mech. Eng.* 323 (2017) 230–249.
- [17] S. Soghrati, A.R. Najafi, J.H. Lin, K.M. Hughes, S.R. White, N.R. Sottos, P.H. Geubelle, Computational analysis of actively-cooled 3D woven microvascular composites using a stabilized interface-enriched generalized finite element method, *Int. J. Heat Mass Transfer* 65 (2013) 153–164.
- [18] M.H.Y. Tan, M. Safdari, A.R. Najafi, P.H. Geubelle, A NURBS-based interface-enriched generalized finite element scheme for the thermal analysis and design of microvascular composites, *Comput. Meth. Appl. Mech. Eng.* 283 (2015) 1382–1400.
- [19] A.R. Najafi, M. Safdari, D.A. Tortorelli, P.H. Geubelle, A gradient-based shape optimization scheme using an interface-enriched generalized FEM, *Comput. Meth. Appl. Mech. Eng.* 296 (2015) 1–17.
- [20] C.A. Brebbia, A.J. Ferrante, *Computational Hydraulics*, Butterworths, London, 1983 Ch. 4.
- [21] M. Bahrami, M.M. Yovanovich, J.R. Culham, Pressure drop of fully-developed, laminar flow in microchannel of arbitrary cross-section, *J. Fluids Eng.* 128 (2006) 1036–1044.
- [22] R.K. Shah, A.L. London, *Laminar Flow Forced Convection in Ducts*, Academic Press, 1978 Ch. 2 and 7, pp. 20 and 200.
- [23] A. Jarrett, Multi-Objective Design Optimization of Electric Vehicle Battery Cooling Plates Considering Thermal and Pressure Objective Functions, Master's Thesis Queen's University, 2011.
- [24] A.R. Najafi, A.M. Coppola, S. Soghrati, N.R. Sottos, S.R. White, P.H. Geubelle, Microvascular composite skin panels for hypersonic aircraft, in: AIAA SciTech 2014 Meeting, Paper AIAA-2014-0630, National Harbor, MD, 2014.
- [25] A.M. Aragón, C.A. Duarte, P.H. Geubelle, Generalized finite element enrichment functions for discontinuous gradient fields, *Int. J. Numer. Meth. Eng.* 82 (2009) 242–268.
- [26] A.M. Aragón, K.J. Smith, P.H. Geubelle, S.R. White, Multi-physics design of microvascular materials for active cooling applications, *J. Comput. Phys.* 230 (2011) 5178–5198.
- [27] A.M. Aragón, R. Saksena, B.D. Kozola, P.H. Geubelle, K.T. Christensen, S.R. White, Multi-physics optimization of three-dimensional microvascular polymeric components, *J. Comput. Phys.* 233 (2013) 132–147.
- [28] W.M. Kays, M.E. Crawford, *Convective Heat and Mass Transfer*, McGraw-Hill, New York, 1993 Ch. 9, p. 115.
- [29] S. Soghrati, A.M. Aragón, C.A. Duarte, P.H. Geubelle, An interface-enriched generalized FEM for problems with discontinuous gradient fields, *Int. J. Numer. Meth. Eng.* 89 (2012) 991–1008.
- [30] S. Soghrati, P.H. Geubelle, A 3D interface-enriched generalized finite element method for weakly discontinuous problems with complex internal geometries, *Comput. Meth. Appl. Mech. Eng.* 217–220 (2012) 46–57.
- [31] S. Soghrati, Hierarchical interface-enriched finite element method: an automated technique for mesh-independent simulations, *J. Comput. Phys.* 275 (2014) 41–52.
- [32] S. Soghrati, H. Ahmadian, 3D hierarchical interface-enriched finite element method: implementation and applications, *J. Comput. Phys.* 299 (2015) 45–55.
- [33] M. Safdari, A.R. Najafi, N.R. Sottos, P.H. Geubelle, A NURBS-based interface-enriched generalized finite element method for problems with complex discontinuous gradient fields, *Int. J. Numer. Meth. Eng.* 101 (12) (2015) 950–964.
- [34] S. Soghrati, J.L. Barrera, On the application of higher-order elements in the hierarchical interface-enriched finite element method, *Int. J. Numer. Meth. Eng.* 105 (6)

- (2015) 403–415.
- [35] P.A.N. Bosman, On gradients and hybrid evolutionary algorithms for real-valued multi-objective optimization, *IEEE Trans. Evol. Comput.* 16 (2012) 51–69.
- [36] Q. Zhang, H. Li, MOEA/D: a multiobjective evolutionary algorithm based on decomposition, *IEEE Trans. Evol. Comput.* 11 (2007) 712–731.
- [37] A. Jaszkiwicz, On the performance of multi-objective genetic local search on the 0/1 knapsack problem, *IEEE Trans. Evol. Comput.* 6 (2002) 402–412.
- [38] K. Deb, S. Agrawal, A. Pratap, T. Meyarivan, A fast and elitist multiobjective genetic algorithm: NSGA-II, *IEEE Trans. Evolut. Comput.* 6 (2002) 182–197.
- [39] B.J. Ritzel, J.W. Eheart, S. Ranjithan, Using genetic algorithms to solve a multiple objective groundwater pollution containment problem, *Water Resour. Res.* 30 (1994) 1589–1603.
- [40] A. Messac, A. Ismail-Yahaya, C.A. Mattson, The normalized normal constraint method for generating the Pareto frontier, *Struct. Multidiscipl. Optim.* 25 (2003) 86–98.
- [41] P.T. Boggs, J.W. Tolle, Sequential quadratic programming, *Acta Numer.* 4 (1995) 1–51.
- [42] C. Le, J. Norato, T. Bruns, C. Ha, D. Tortorelli, Stress-based topology optimization for continua, *Struct. Multidiscipl. Optim.* 41 (2010) 605–620.
- [43] T.M. Bandhauer, S. Garimella, T.F. Fuller, A critical review of thermal issues in lithium-ion batteries, *J. Electrochem. Soc.* 158 (3) (2011) R1–R25.